# Microstructural characterization and thermal stability of He charged amorphous silicon films prepared by magnetron sputtering in helium

A. Fernández, T. Sauvage, B. Diallo, D. Hufschmidt, M.C. Jiménez de Haro, O. Montes, J.M. Martínez-Blanes, J. Caballero, V. Godinho, F.J. Ferrer, et al.

Materials Chemistry and Physics 301 (2023) 127674

Contents lists available at ScienceDirect

Materials Chemistry and Physics

journal homepage: www.elsevier.com/locate/matchemphys

# Microstructural characterization and thermal stability of He charged amorphous silicon films prepared by magnetron sputtering in helium

A. Fernández [a,d,*], T. Sauvage [b,**], B. Diallo [b], D. Hufschmidt [a], M.C. Jiménez de Haro [a], O. Montes [a], J.M. Martínez-Blanes [a], J. Caballero [a], V. Godinho [a], F.J. Ferrer [c], S. Ibrahim [d], P. Brault [d], A.-L.- Thomann [d]

[a] Instituto de Ciencia de Materiales de Sevilla (CSIC-Univ. Seville), Avda. Américo Vespucio 49, 41092, Sevilla, Spain
[b] CEMHTI, UPR3079 CNRS, 1D avenue de la Recherche Scientifique, 45071, Orléans, France
[c] Centro Nacional de Aceleradores (Univ. Sevilla, J. Andalucía, CSIC), Av. Tomás Alva Edison 7, 41092, Seville, Spain
[d] GREMI, UMR7344 CNRS Université d'Orléans, 14 rue d'Issoudun, 45067, Orléans, France

## HIGHLIGHTS

- Si sputtering in He to produce amorphous silicon films containing gas filled nanopores.
- A maximum He/Si atomic ratio of 0.9 has been achieved.
- Determination of microstructure and composition for different deposition conditions.
- He release starts at 573–723 K annealing temperature for ca. 30 at% He content.
- Tuning from solid-gas ($^4$He and $^3$He) nanocomposites to nano-porous amorphous silicon films.

## GRAPHICAL ABSTRACT

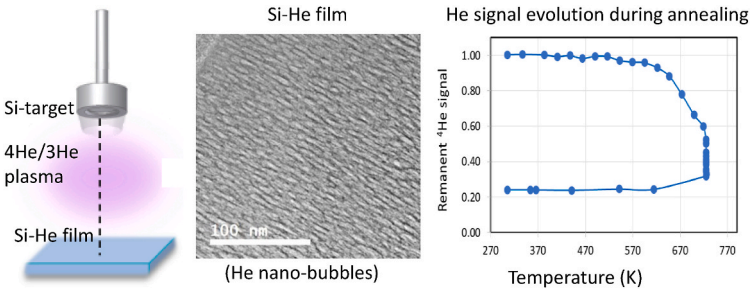


## ARTICLE INFO

*Keywords:*
Magnetron sputtering in helium
4He and 3He charged Si films
Microstructural characterization
IBA analysis
Thermal stability for He release
Nanopores and nanobubbles

## ABSTRACT

Sputtering of silicon in a Helium magnetron discharge has been reported as a bottom-up procedure to obtain amorphous Si films containing high amounts of gas-filled nanopores. Here we compare the microstructure and composition of Si–He nanocomposite films deposited by magnetron sputtering (MS) with $^4$He in DC or RF and $^3$He in RF operation modes. Electron microscopy (SEM and TEM), X-ray diffraction (XRD) and ion beam analysis (IBA) have been used to analyze the films and to investigate the *in-situ* and *ex-situ* thermal evolution. Depending on deposition conditions different in depth compositions, nanopore size and shape distributions, porosity and He content could be obtained. The presence of impurities (i.e. oxygen) has shown to promote He diffusivity reducing He accumulation. The start temperature of He-release varied in the range 473–723 K without films crystallization. Films grown in RF mode reached contents of 32 and 29 at% of $^4$He and $^3$He and were respectively stable up to 573 and 723 K both in vacuum and under inert gas flow. *In-situ* p-EBS (proton Elastic Back Scattering) allowed monitoring the He release accompanied by blistering/delamination effects visualized by SEM. These results show the potentiality of annealing to hold nano-porous structures after liberation of trapped gas.

* Corresponding author. Instituto de Ciencia de Materiales de Sevilla (CSIC-Univ. Seville), Avda. Américo Vespucio 49, 41092, Sevilla, Spain.
** Corresponding author.
*E-mail addresses:* asuncion@icmse.csic.es (A. Fernández), thierry.sauvage@cnrs-orleans.fr (T. Sauvage).

https://doi.org/10.1016/j.matchemphys.2023.127674
Received 21 January 2023; Received in revised form 7 March 2023; Accepted 24 March 2023
Available online 28 March 2023

## 1. Introduction

Irradiation of metals with high to low energy (500 keV–100 eV) ion beams of light elements, and in particular He, has been a subject of study for many years due to its technological interest to study damage in nuclear reactor materials [1–6]. It was found that the dominating feature of inert gas atoms implanted in most solids is their high heat of solution, leading in most situations to an essentially zero solubility and gas-atom precipitation (formation of small "bubbles") [7–9]. In addition to ion bombardment, helium plasma surface interaction experiments [10,11] and magnetron sputtering in He/Ar mixtures [12–14] also reported He incorporation, porosity and bubbles formation in different metals. The introduction of helium bubbles (cavities) by ion implantation found applications in silicon technology [15]. First experiments using magnetron sputtering (MS) of Si in pure He [16] showed the formation of Si thin films presenting closed nanoporosity and containing large amounts of trapped He. High resolution analytical transmission electron microscopy (TEM) allowed to demonstrate bubble formation by location of the He inside the nanopores at high pressure [17]. Gas charged films have been also reported for trapped $N_2$ [18,19] and He [20,21] in different matrix elements fabricated by the magnetron sputtering "bottom-up" process in pure $N_2$ and He plasmas. Versatility, scalability and low cost are advantages of the sputtering methodology.

Over the past years interesting applications have been arising for the amorphous Si–He nanocomposite films based on their particular characteristics. Considering the high amount (up to 44 at% previously reported [22]) of stable trapped helium, films were proposed as solid $^4$He or $^3$He targets for nuclear reaction studies in inverse-kinematic configuration and cross-section measurements [22–25]. These targets can overcome limitations of cryogenic or gas cell-based systems, which are bulky and difficult to handle thus facilitating usage, reducing energy straggling effects and simplifying geometry for calculations. Due to the films nanoporosity they were also proposed for single-material optical devices fabrication by alternating nanoporous and dense silicon layers with on-demand controlled refractive index [26]. The closed *vs* conventional open porosity in porous silicon makes the devices very stable against chemical environments [26]. The closed nanoporous silicon material has been also tested as anode for all-solid-state lithium batteries [27]. Improved capacity and stability upon lithiation-delithiation cycling was found due to favoured relief of deformation-induced stress probed in the closed nanoporous silicon [27]. Building on the perspective interest and potential applications in different fields the present article aims to investigate the thermal stability and evolution of the amorphous Si–He nanostructured films grown by bottom-up MS deposition. Both the permanence of He trapped and the structural evolution of the nanoporous microstructure will be considered. Previous annealing experiments were reported in He implanted metals in relation to irradiation damage in nuclear reactor materials [28]. Studies have been also reported for He implanted crystalline Si in relation to cavities and nanocavities formation of interest in silicon technology [29–31]. New studies are presented here for the case of amorphous Si–He nanocomposite films charged with high amounts of trapped He distributed along the films thickness as fabricated in a He magnetron discharge.

Films were grown by MS with $^4$He and $^3$He in DC or RF operation modes aiming to evaluate the relationship between microstructure, composition and the thermal stability. Microstructural characteristic were referred to nanopore size and shape distributions, in depth He incorporation (Si/He atomic ratios) and total porosity. Significant experiments to monitor the *in-situ* He releases were done by ion beam analysis (IBA) in a dedicated chamber [32] during annealing in vacuum. Ex-situ annealing was also done under inert gas (Helium) flow conditions for complementary experiments. A variety of characterization techniques including electron microscopy (TEM and SEM) and complete IBA analysis (He, Si and possible impurities as O, C or H) are reported. The presented work aims to determine optimized films preparation conditions for high helium content and stability under annealing. Also a goal in this work was to evaluate structural damages and/or potentiality of the nanocomposite materials to hold the nanoporous structure after annealing. These results with silicon based films would be also a reference in the context of further investigations regarding "solid-gas" nanocomposite materials with other gases and matrix elements.

## 2. Experimental

### 2.1. Films preparation

The $^4$He and $^3$He charged Si films were prepared within a conventional magnetron sputtering (MS) deposition chamber (residual vacuum in the range $1\times10^{-6}$ mbar) to operate with one magnetron head furnished with a 2 inch Si cathode (from Neyco, 99.999% purity). The cathode was placed parallel to the substrate holder at a distance of 10 cm. As process gases we used: (i) natural He (mainly $^4$He) as supplied by Air Liquide (99.999% purity) and (ii) enriched $^3$He as received from Chemgas (≥99.9% purity). A detailed description of the deposition chamber can be found in Refs. [24] and [33]. In particular details are described for conditions of very low consumption of the scarce and expensive $^3$He gas.

Table 1 summarizes the nomenclature of main three investigated samples along with their deposition parameters: deposition time, substrate(s), gas pressure, power, discharge voltage, substrate temperature and evaluated deposition rates. Samples 1 and 3 were grown in a RF discharge using a magnetron ION'X from the TFC (Germany) Company. For sample 2 a magnetron from the AJA (USA) Company was employed in DC mode. Power generators CesarRF-Dressler and Advance Energy-Pinnacle Plus were respectively used in RF and DC mode and operated with constant power. The sample holder is at floating potential and was not cooled. To estimate and monitor the substrate temperature during film growth, a thermocouple is placed in a lateral zone of the sample holder a few millimeters above the surface. The films were synthesized as coatings on silicon wafer (100) substrates of 525 μm thickness. Only for specific XRD analysis in Bragg-Brentano configuration (Figs. 8 and 9) also fussed quartz substrates of 0.5 mm thicknesses were used as provided from Neyco.

An additional Si–He-RF sample (nr. 4, Si–He-RF/fl) was fabricated for complementary experiments of ex-situ annealing under inert gas flow conditions. This sample was fabricated on Si and fussed quartz substrates at 150W in RF mode in a chamber with a 30° tilted magnetron placed at 5 cm vertical distance to the sample holder. Details can be

**Table 1**
Nomenclature and deposition parameters for main investigated samples.

| Sample nr. Description | Deposition time | Substrate | $^4$He or $^3$He pressure (Pa) | Power (DC or RF) (W) | Discharge voltage[a)] (V) | Substrate temperature (K) | Deposition rate[c)] (nm/min) |
|---|---|---|---|---|---|---|---|
| **1**: Si–He-RF | (4h) | Si, $SiO_2$ | 4.8 | 150 (RF) | 197–205 | 473–487 | 7.1 ± 0.05 |
| **2**: Si–He-DC | (4h) | Si | 4.8 | 100 (DC) | 395 | 863–673[b)] | 7.3 ± 0.05 |
| **3**: Si–$^3$He-RF | (4h) | Si | 5.0 | 150 (RF) | 170–180 | 473–483 | 5.4 ± 0.1 |

[a] Measured voltage in the sources working at constant power (cathode voltage in DC or self-bias in RF).
[b] A higher temperature was observed at the starting of deposition for this sample.
[c] Calculated from deposition time and the thickness determined by SEM.

**Table 2**
Annealing conditions for thermal stability studies.

| Sample nr. Description | "In-situ" p-EBS analysis(Annealing under vacuum)(Films substrate: Silicon wafer) | | "In-situ" XRD analysis(Annealing under vacuum)(Film substrate: Fussed quartz) | | "Ex-situ" XRD analysis(Annealing under a Helium flow of 100 ml/min)(Film substrate: Fussed quartz) | |
|---|---|---|---|---|---|---|
| | Heating ramp 10K/min | Isothermal annealing at final T | Heating ramp (10K/min) in 100° steps | Isothermal annealing at each step | Heating ramp 10 K/min | Time of isothermal annealing |
| **1**: Si–He-RF | R.T.[a)]-723K | 60 min. | 373K–1473K | 4–5 min | | |
| **2**: Si–He-DC | R.T.-723K | 30 min. | | | | |
| **3**: Si–$^{3}$He-RF | R.T.-773K | –[b)] | | | | |
| **4**: Si–He-RF/fl | | | | | R.T.-573K | 120 min. |
| | | | | | R.T.-823K | 120 min. |

[a] R.T. room temperature.
[b] No isothermal annealing to avoid detector damage.

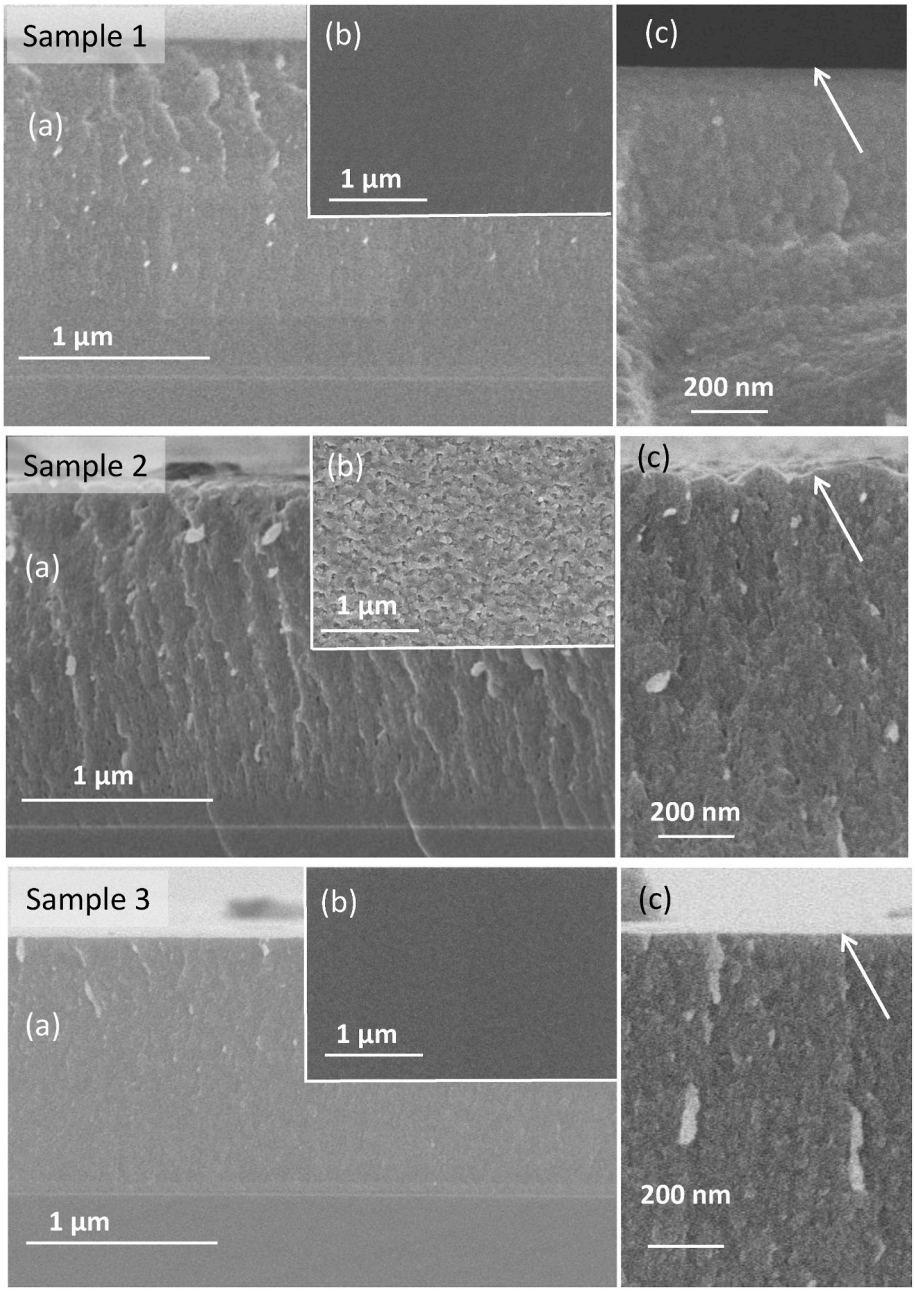


**Fig. 1.** SEM images of samples 1 to 3: (a) Low magnification cross-section; (b) planar view; (c) high magnification cross sections at the top (arrows remark the surface rugosity differences).

**Table 3**
Area density of Si and He and average porosity for the total thickness of investigated Si layers.

| Sample nr. Description | Thickness[a)] (μm) | Area density ($10^{15}$ at/cm$^2$) | | | Atomic ratio $^4$He/Si | Atomic ratio $^3$He/Si | Porosity (%) |
|---|---|---|---|---|---|---|---|
| | | $^4$He | $^3$He | Si | | | |
| **1**: Si–He-RF | 1.70 ± 0.05 | 3540 | – | 5900 | 0.60 | – | 29 ± 1 |
| **2**: Si–He-DC | 1.75 ± 0.06 | 3730 | | 6320 | 0.59 | – | 26 ± 1 |
| **3**: Si–$^3$He-RF | 1.3 ± 0.1 | – | 1950 | 4430 | – | 0.44 | 30 ± 2 |

[a] Measured from SEM cross-section (at different positions and cleaved areas).

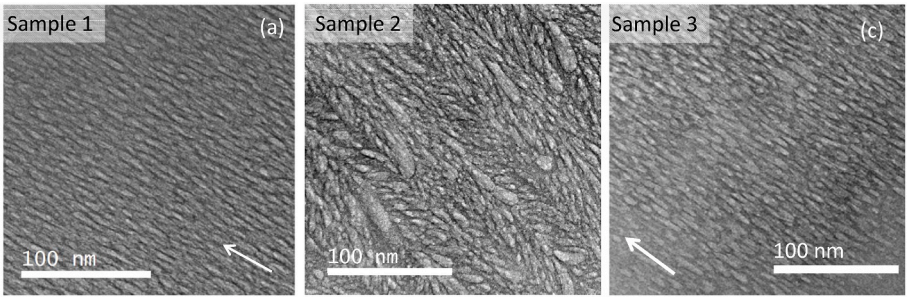


**Fig. 2.** TEM cross section images of samples 1 to 3. The arrows indicate the film growing direction.

**Table 4**
Average elemental composition for the total thickness of investigated Si layers.

| Sample nr. Description | at% Si | at% $^4$He | at% $^3$He | at% O | at% C | at% H |
|---|---|---|---|---|---|---|
| **1**: Si–He-RF | 54 | 32 | – | 3,6 | 2.3 | 8.4 |
| **2**: Si–He-DC | 54 | 32 | – | 4.9 | 0.5 | 8.7 |
| **3**: Si–$^3$He-RF | 65 | – | 29 | 1.6 | 1.9 | 2.6 |

found in supporting information (Fig. S1).

### 2.2. Films characterization (microstructure and composition)

The thickness and morphology of the films (before and after annealing) were examined by scanning electron microscopy (SEM) by employing a HITACHI S-4800 SEM-FEG microscope operated at 1–2 kV. The samples deposited on silicon substrates were observed as such in top views and additionally cleaved for cross-sectional views. The nanostructure of the nanocomposite films was investigated at the Laboratory of Nanoscopies and Spectroscopies (LANE-ICMS, Sevilla, Spain) by Transmission Electron Microscopy (TEM) using a Jeol 2100Plus and a Tecnai G2 F30 TEM operated at 200 and 300 kV, respectively. The cross sectional TEM lamellas were prepared by mechanical polishing and dimple grinding of the coatings deposited on silicon, followed by $Ar^+$ ion milling to electron transparency. Low angle ion milling and polishing were carried out in a Fischione Instrument of Model 1010. Representative porous areas were selected for imaging and analysis. The pore distribution was evaluated from TEM micrographs by binarizing them and using the "Analyze Particle" function of imageJ software [34].

The presence of crystalline phases in films grown on Si substrates (before and after annealing) was investigated by X-Ray diffraction (XRD) analysis using a Bruker D8 Discover X-ray diffractometer in grazing incidence geometry operated with Cu Kα radiation. For details of particular "in-situ" and "ex-situ" XRD analysis we refer to section 2.3.

The elemental and in depth composition of the coatings were determined by IBA (Ion Beam Analysis) at the Pelletron accelerator of CEMHTI laboratory (Orléans), a facility that is part of the EMIR&A French network of accelerators (http://emir.in2p3.fr). The 3U-2 Pelletron is a 3 MV single-ended electrostatic accelerator from National Electrostatic Corporation company (NEC). Target currents are in the range of 0.5 nA to a few tens μA.

Silicon films grown on silicon substrates were measured as received recording IBA spectra as follows.

i) Proton-beam at 2400 keV, 0° incidence angle and 178° scattering angle. For sensitivity to 4-helium by proton-Elastic Backscattering Spectrometry (p-EBS)
ii) α-beam at 2950 keV, 75° incidence angle and 30° scattering angle. For sensitivity to hydrogen by Elastic Recoil Detection Analysis (ERDA)
(iii) α-beam at 2950 keV, 75° incidence angle and 155° scattering angle. For sensitivity to silicon by Rutherford Backscattering Spectrometry (RBS)
(iv) Deuteron-beam at 1550 keV, 0° incidence angle and 166° scattering angle. For sensitivity to oxygen and carbon by Nuclear Reaction Analysis (NRA)
(v) Deuteron-beam at 900 keV, 0° incidence angle and 178° scattering angle. For sensitivity to 3-helium, oxygen and carbon by Nuclear Reaction Analysis (NRA)

Spectra i) to iv) were used to analyze samples 1 and 2. For sample 3 spectrum iv) was replaced by spectrum v). The four selected IBA spectra for each sample were simulated by SIMNRA software [35] to obtain a unique target structure solution with concentration gradients of all detected elements. The nuclear reactions differential cross-sections are provided from SigmaCalc [36] and IBANDL databases [37]. Complete experimental conditions can be found in the supporting information section (Figs. S2–S5). Elemental depth resolution and detection limits for the IBA analysis are included in Fig. S6 what also accounts for the accuracy of quantifications.

Elemental areal densities in at.cm$^{-2}$ and in depth compositions were quantified for Si, incorporated He and possible contaminant elements (H, O, C) as present on the films after magnetron sputtering preparation. Films total thickness, as determined by SEM, together with in depth IBA analysis and the reported density for amorphous silicon [38] have been used for porosity rate estimations.

### 2.3. Annealing experiments

Thermal stability experiments were done for all samples included in Table 1 by annealing in vacuum in the dedicated DIADDHEM chamber [32] at the Pelletron accelerator of CEMHTI laboratory. PEBS spectra

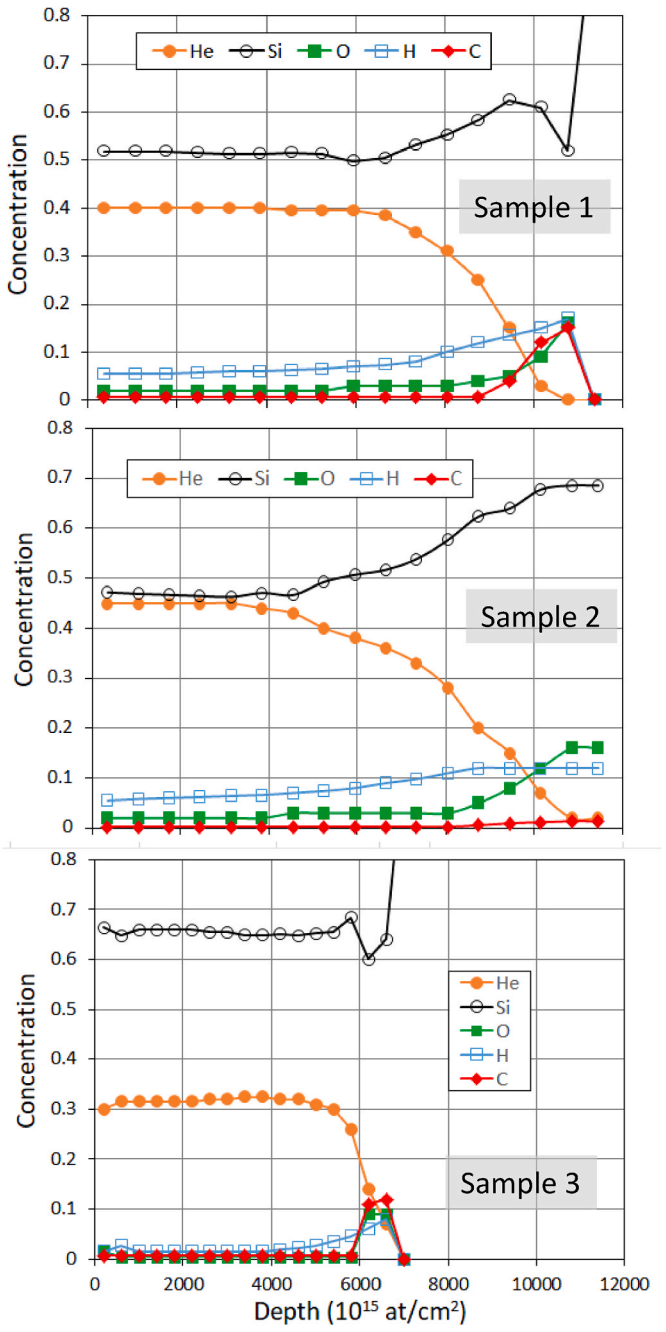


**Fig. 3.** Elemental depth profiles derived from total-IBA analysis (i.e. combining various beam conditions as described in the experimental section) for samples 1 to 3.

were *in-situ* recorded each 1.5 min with a 2.4 MeV protons beam during continuous heating starting from room temperature with a 10 K/min ramp. Depending on the kinetic of He release final temperature and isothermal annealing were selected and summarized in Table 2. For samples 1 and 2 a continuous heating ramp was done up to 723 K with isothermal annealing of 60 min for sample 1 and 30 min for sample 2. Sample 3 was heated up to 753 K with the continuous ramp and then cooled to avoid detector damage. Cooling was done with a 30 K/min ramp down to 373 K. Residual vacuum during experiments was in the range $10^{-7}$ to $4.10^{-7}$ mbar. Sample 1 (Si–He-RF) was also selected for *in-situ* X-ray diffraction analysis during annealing in vacuum (see conditions in Table 2). A PANalytical X'Pert PRO diffractometer, equipped with a HTK-1200 N heatable chamber from Anton-Paar, was used in

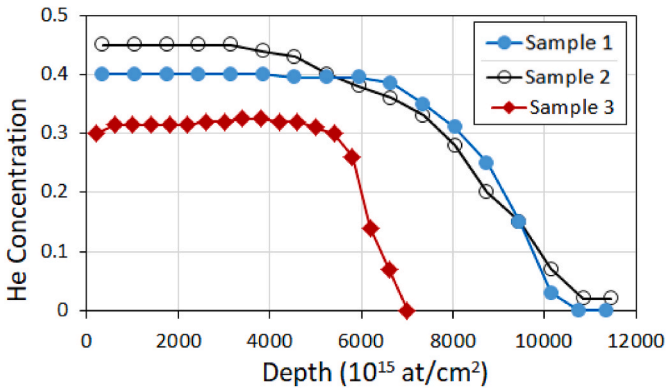


**Fig. 4.** Helium elemental depth profiles derived from: (i) proton beam EBS-spectra for $^4$He in samples 1 and 2; (ii) deuteron beam NRA-spectra for $^3$He in sample 3.

**Table 5**
Characterization of top part of the films with constant He concentration.

| Sample nr. Description | % of total depth[a] | Area density ($10^{15}$ at/cm$^2$) | | | at% $^4$He ($^4$He/Si atomic ratio) | at% $^3$He ($^3$He/Si atomic ratio) |
|---|---|---|---|---|---|---|
| | | $^4$He | $^3$He | Si | | |
| **1**: Si–He-RF | 59 | 2780 | | 3590 | 40 (0.75) | |
| **2**: Si–He-DC | 46 | 2730 | | 2990 | 45 (0.90) | |
| **3**: Si–$^3$He-RF | 80 | | 1765 | 3660 | | 30 (0.50) |

Determined from TFU units (1015 at/cm2) depth profiles.
[a] Percentage of total depth showing constant He concentration.

Bragg-Brentano configuration. Diffractograms were registered for samples prepared onto fussed quartz substrates at selected temperatures from 373 to 1473 K in 100° steps. Heating was done with a ramp of 10 K/min to reach the desired T value. In each step the temperature was maintained for 4.5 min (adequate time for diffractogram recording).

Complementary ex-situ annealing experiments were also done under inert gas flow (see conditions in Table 2). The additional films (sample nr.4, Si–He-RF/fl) deposited on silicon and fussed quartz substrates were heated in a tubular furnace Thermolyne 59300 in a He flow of 100 ml/min. A 10 K/min ramp was used until the desired temperatures of 573 and 823 K were reached and maintained for 120 min annealing time. After stopping heating the samples were cooled to room temperature inside the furnace under the He flux. The as prepared and ex-situ annealed films deposited on $SiO_2$ were analyzed by XRD using a PANalytical X'Pert PRO diffractometer with Cu Kα radiation in Bragg-Brentano geometry. The films deposited on Si were analyzed ex-situ by p-EBS at the 3 MV NEC 9SDH-2 tandem accelerator of the National Centre for Accelerators (CNA, Seville, Spain) using a 2.0 MeV proton beam and a passivated implanted planar silicon (PIPS) detector set at 165°.

## 3. Results and discussion

### 3.1. The as-prepared samples

Fabrication of Si based films has been undertaken in pure Helium plasmas with the MS deposition conditions summarized in Table 1 and described in the experimental section. Sample 1 represents the film obtained with $^4$He in RF mode while sample 2 corresponds to $^4$He in DC. Sample 3 is representative of $^3$He loaded films prepared in RF mode. Fig. 1 presents SEM electron microscopy studies of the as-prepared samples. The low magnification SEM cross section images (a) were

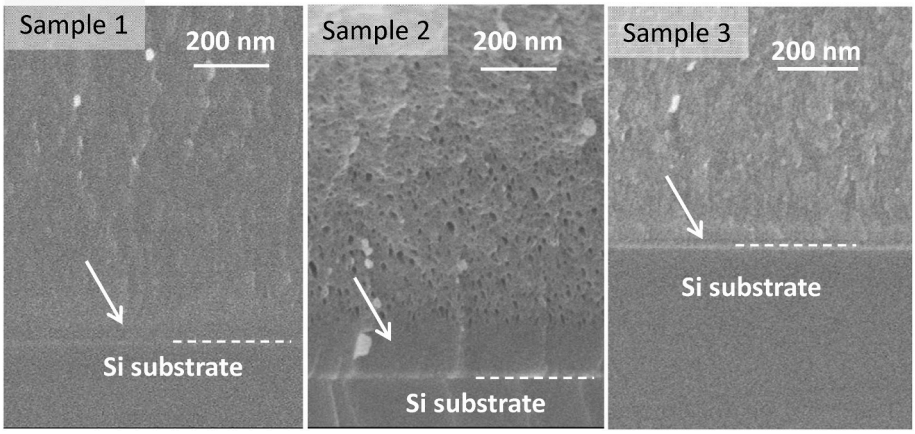


**Fig. 5.** High magnification SEM cross sections images near the substrate for samples 1 to 3.

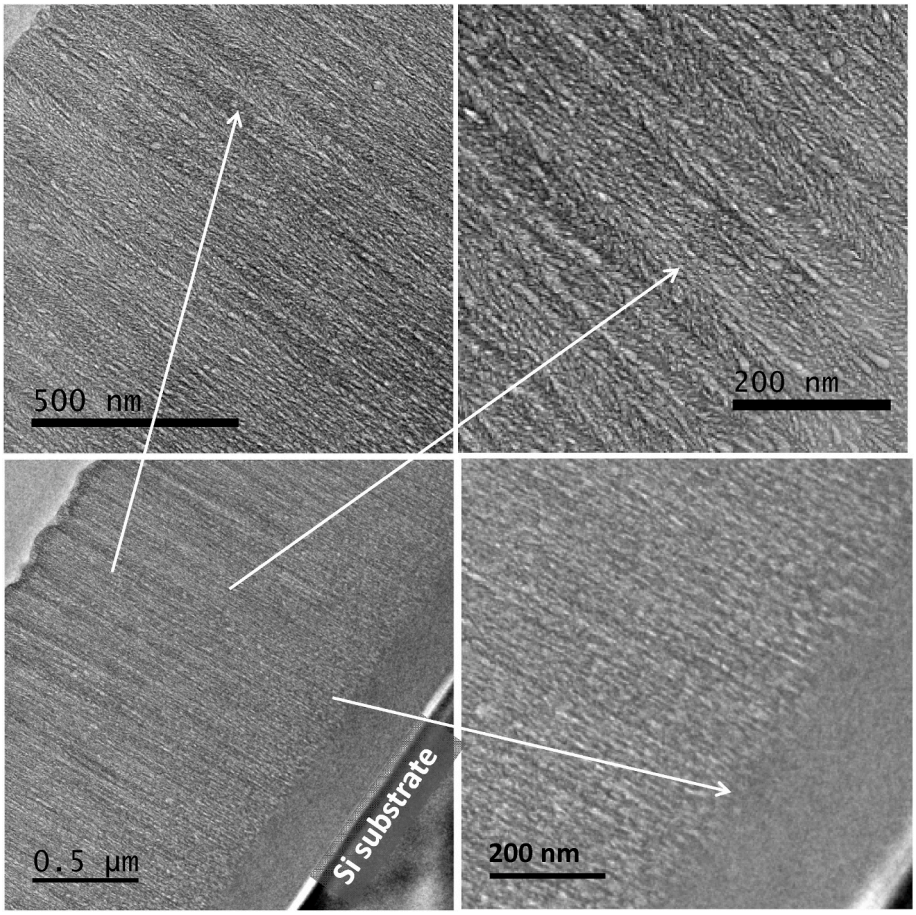


**Fig. 6.** TEM cross section images of sample 2. Low magnification at bottom-left. High magnification at indicated zones. A dense thin layer at the first stage of film growth is visualized at bottom-right.

first used to determine the films thicknesses and therefore the deposition rates summarized in Tables 3 and 1 respectively. For the RF mode in same conditions a lower deposition rate was determined for the low atomic mass $^{3}$He as compared to $^{4}$He due to the expected lower sputtering rate [39]. Deposition conditions in DC and RF for $^{4}$He were selected to get comparable deposition rates. For a working pressure of 4.8Pa, and same geometrical parameters, it was necessary to reduce the discharge power from 150W in RF to 100W in DC. Even so quite higher discharge voltage and substrate temperature were measured during DC deposition as compared to RF (Table 1). This will affect the films microstructure as will be discussed below.

SEM images in Fig. 1 also show planar views (b) and cross-sections from the top part (c) of the investigated samples. The layer grown in DC (sample 2) shows a notorious surface nanostructuration as compared to the RF ones (samples 1 and 3). High magnification TEM images in Fig. 2, obtained from representative porous areas of cross-section lamellas, clearly show the characteristic nanoporous structure of the He containing films which tend to align in the growing direction (indicated by the arrows in Fig. 2). The DC sample show broader pore size and shape distributions in comparison to the RF ones in agreement with the

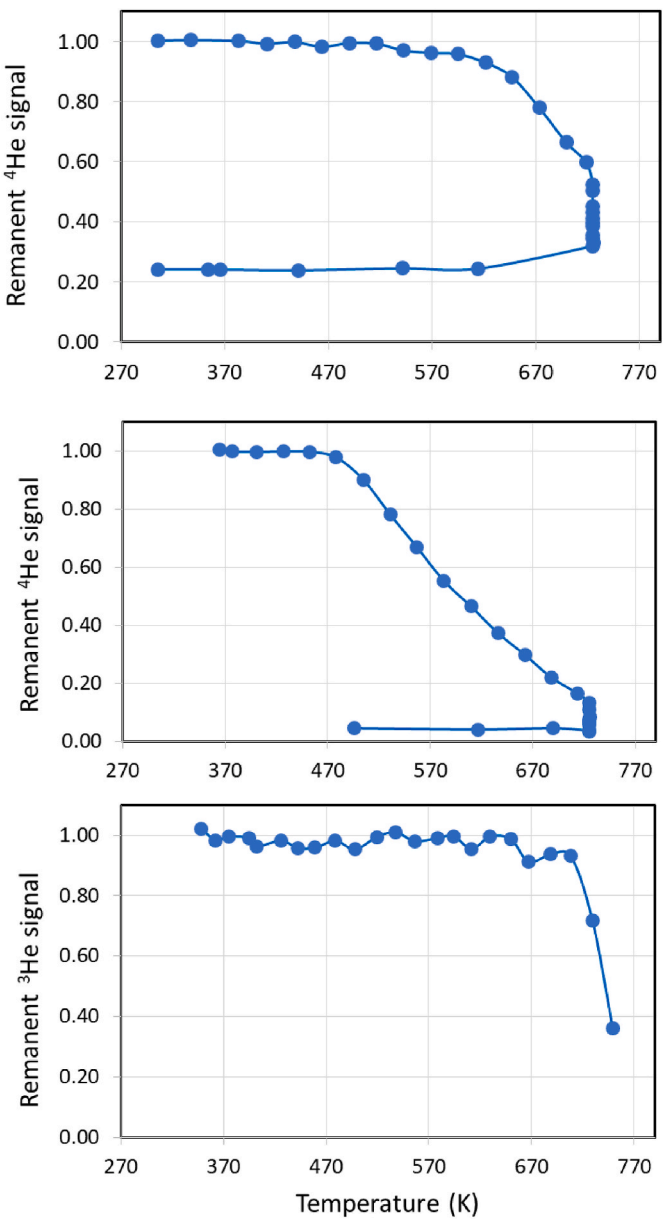


**Fig. 7.** Helium content evolution derived from proton EBS-spectra during *in-situ* annealing in vacuum at indicated temperatures for samples 1 to 3.

surface nanostructuration observed in SEM. Pore size and aspect ratio histograms are reported in supporting information together with the details of TEM image analysis (Fig. S7 a and b). Both deposition regimes and isotopes lead to different pore size and shape distributions. For samples synthesized by RF mode the pores were identified in the range of 0.5–15 and 5–20 nm for $^4$He and $^3$He respectively also associated to the different deposition rates. For the $^4$He DC sample most abundant pores are of 0.5–15 nm with additional pores from 15 to 30 nm showing also a broader pore shape distribution as compared to RF samples. Registered discharge voltage and substrate temperature values during films fabrication are reported in Table 1 with the sources operating in constant power mode. The higher deposition temperature reached in DC as compared to RF, in the present experimental conditions, could suggest a transition from zone T to zone 2 in the well-known SZM (structure zone model) diagram as described by A. Anders [40]. This could explain the changes of the microstructure, i.e. turning from densely packed fibrous grains to sharp-edge columnar grains. Nevertheless the presence of trapped He certainly affects the microstructure of the Si films through the bubbles formation. He incorporation and mobility due to higher deposition temperature may also play a role.

Grazing incidence XRD analyses for films grown on Si substrates show in all cases no diffraction peaks as expected for the amorphous nature of the nanostructured Si films [16]. A representative diffractogram from sample 2 is shown in Fig. S8 (supporting information).

A main point in the characterization of the as prepared samples is the determination of He and Si contents by IBA techniques, and their comparison among the different growth conditions. Table 3 shows the absolute determination of He and Si area densities given in $10^{15}$ atom/cm$^2$ (TFU units) for the total film thicknesses of as prepared samples. Atomic He/Si ratios have been also included in the table. The high amounts of stable trapped helium have been demonstrated, both in DC and RF operation modes, showing the suitability of the films to be used as solid $^4$He and $^3$He targets for nuclear reaction studies [22–25]. Considering the total Si areal densities and film thicknesses, the mean porosity of the films has been evaluated and also included in Table 3.

Another point of interest is to evaluate the impurities content of the films coming from plasma activated species from residual vacuum and degassing during operation of the MS chamber. In particular C, O and H are main impurities which have been analyzed by IBA techniques with detection limits summarized in supporting information (Fig. S6). Table 4 shows the elemental composition in atomic percentage for the total thickness of the investigated films showing H and O as main contaminants and also C. The higher discharge voltage and substrate temperature reached in DC may enhance degassing, especially at the initial steps of deposition, leading to the higher H and O content for sample 2.

A main characteristic of the IBA techniques is also their capabilities for in depth analysis which has been demonstrated of particular relevance in this study. Elemental depth profiles derived from IBA are presented in Fig. 3 for the as prepared samples. The results clearly show that the incorporation of hydrogen and oxygen (and also C) occurs mainly at the beginning of the film growth and certainly from degassing species activated by plasma. Their presence would promote He diffusivity and therefore reducing He accumulation, as reported in He implanted silicon oxycarbide [41], oxide [42,43] and hydrogenated amorphous silicon [44]. Fig. 4 shows the comparison of He depth profiles for samples 1 to 3. The decrease of He concentration starts at a lower depth for sample 2 ($4\times10^{18}$ at .cm$^2$) compared to sample 1 ($6\times10^{18}$). Higher substrate temperature at DC plasma conditions are producing a more prolonged degassing at the beginning of the growth associated to H and O incorporation (Fig. 3). After contaminants removal under operation the top layer growths with constant He contents as high as 45 and 40 at % for samples 2 and 1 respectively. The Si:$^3$He film (RF/static) appears particularly homogeneous in depth with the lowest incorporation of O and H contaminants (Figs. 3 and 4) associated to low substrate temperature and the corresponding better residual vacuum.

According to data in Fig. 4 it was also possible to evaluate the % of layer depth at the top part of the films with constant He concentration associated to low amounts of contaminants. Note that these depth percentages, included in Table 5, are determined from depth profiles in TFU units ($10^{15}$ at/cm$^2$). This is not directly related to the thickness in microns as composition and/or porosity may change along the films profile. The Si and He areal densities and the He/Si atomic ratios are presented in Table 5 for this part of the films with constant He concentration. Enhanced He incorporation in comparison to average values in Table 3 are clearly observed for samples 1 and 2. The He/Si atomic ratio of 0.9 at the top layer in sample 2 is the highest value reported, as far as we know, for the Si–He nanocomposite materials fabricated by the MS bottom-up methodology.

To visualize the microstructure associated to the observed gradient He incorporation, cross section SEM images are presented in Fig. 5 for near substrate areas. At the very first stage of the film growth a dense (non-porous) layer is observed associated to Si and the highest contaminants values (O, H, C) with almost zero He trapped. This layer (in the range of 170 to 70 nm thickness) is clearly visible in sample 2 with an

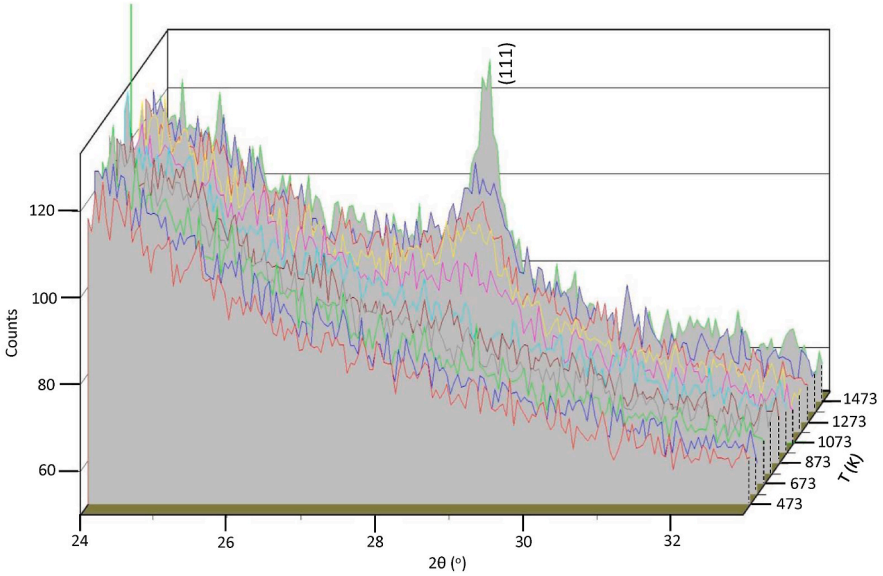


**Fig. 8.** X-ray diffraction evolution for sample 1 during *in-situ* annealing in vacuum at indicated temperatures.

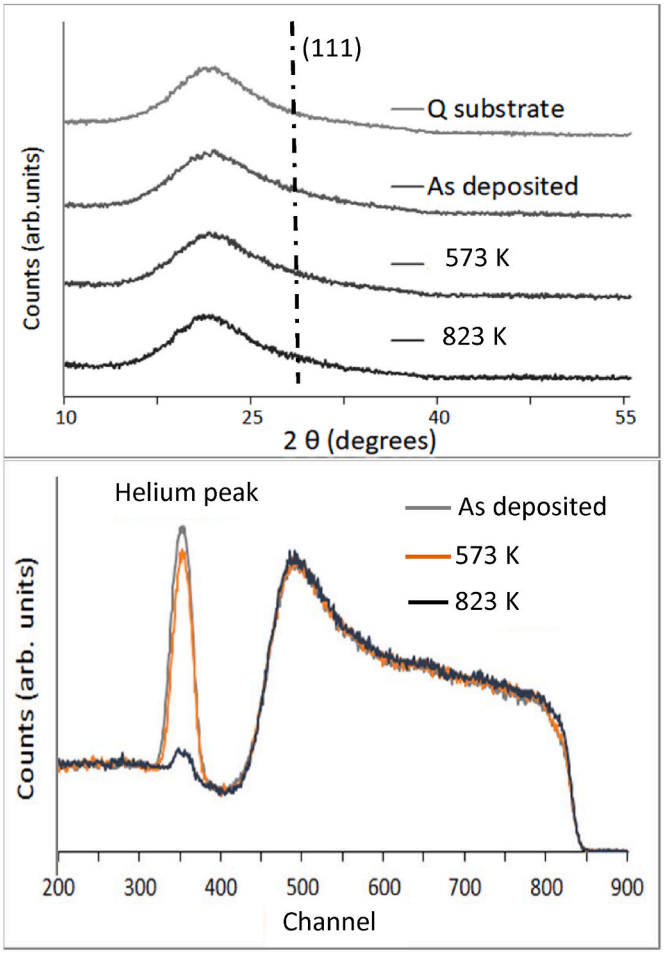


**Fig. 9.** Characterization of sample 4 before and after ex-situ annealing under He flow at indicated temperatures. (Bottom) p-EBS spectra. (Top) X-ray diffraction pattern. XRD pattern for the fussed quartz substrate is also shown.

abrupt change to a highly porous microstructure characteristic of He containing films. If we consider the continuous impurities reduction and Helium incorporation along a much longer distance (Figs. 3 and 4 for sample 2), we can conclude that the growing process may lead to porous structures ranging from empty to He filled pores. This is also congruent with the increasing of He diffusivity and release associated to the amount of impurities in the silicon matrix. A TEM cross-sectional study is presented in Fig. 6 for sample 2 showing the thin dense underlayer near the substrate and the growth of the porous layer from almost empty to He filled pores according to He profiles in Fig. 4. Similar results were found for sample 1 as shown in supporting information (Fig. S9). In this figure it is also remarkable the formation of highly elongated pores aligned into the growing direction.

It is worth to emphasize that the exhaustive microstructural and compositional characterization of the films presented in this section provided new data to understand limitations, and to improve tailored fabrication, of Si–He nanocomposite films by MS in He atmospheres.

### 3.2. *"In-situ" and "ex-situ" annealing*

For a practical use of the He charged films it is important to elucidate the prevalence of micro-structure and/or composition of the He-charged films under manipulation and use. In particular a main objective in this work was to investigate the evolution of the Si–He films under annealing in vacuum or inert gas atmosphere. Thermal helium desorption in He implanted silicon has been widely investigated. Oliviero et al. [45] described Helium release from bubbles/cavities in silicon by the permeation from cavities to the surface. Nguyen et al. [46] studied the formation and growth of nanocavities and cavities by $He^+$ implantation followed by a $N_2$ ambient annealing at 1073 K. Alix et al. [47] studied the evolution of helium nanobubbles during in situ annealing probed by spectrum imaging in the transmission electron microscope. They showed that helium emission takes place at temperatures where bubble migration had hardly started. At higher temperatures, the migration (and coalescence) of voids is clearly revealed. A dedicated study for the He–Si nanocomposite films prepared by the bottom-up MS deposition was not previously reported. These results may also be of interest to understand He distributions along the complete films thickness as prepared by MS under the experimental conditions investigated in the present work.

Fig. 7 shows the *in-situ* measured evolution of He content during heating in vacuum for samples 1 to 3 (see Table 2 for annealing

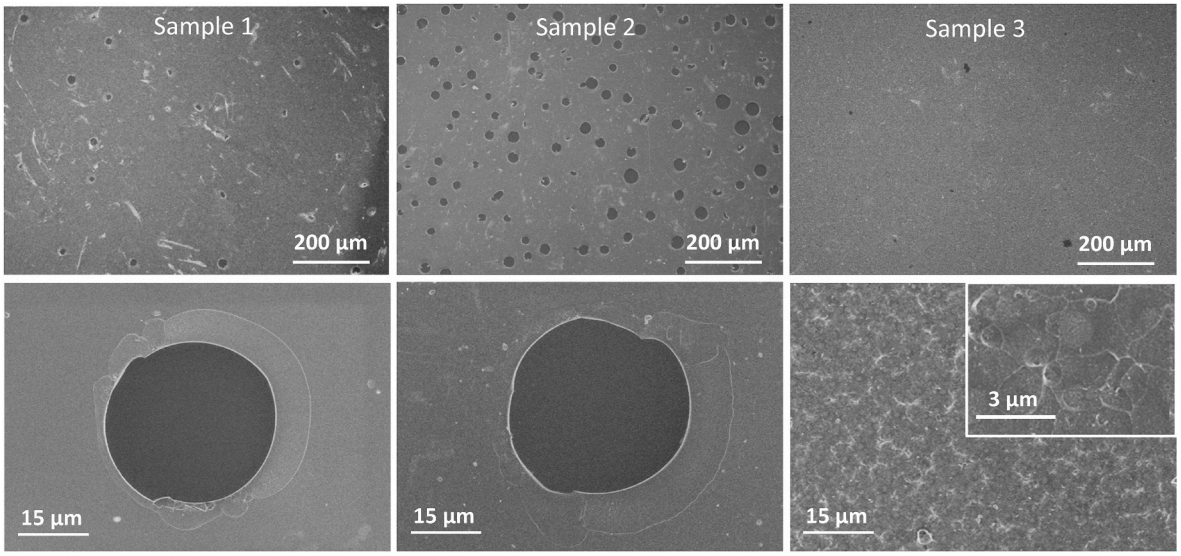


**Fig. 10.** SEM images in top-view for samples 1 to 3 after in-situ annealing: (top) low magnification; (bottom) high magnification.

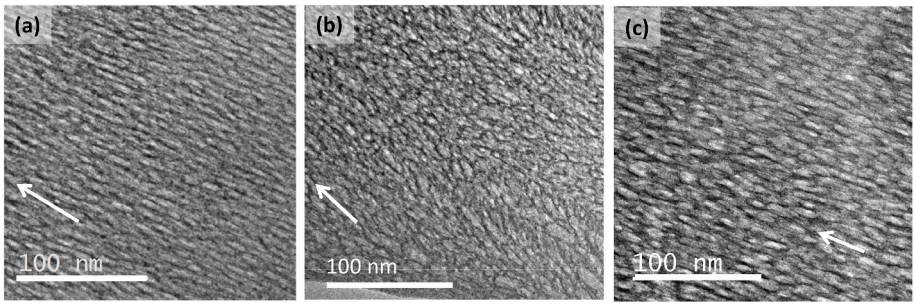


**Fig. 11.** TEM cross section images for samples 1 to 3 after in-situ annealing.

conditions). Sample 2 (grown in DC) is showing He desorption starting at 473 K while samples 1 and 3 (grown in RF) show the onset at 573 and 723 K respectively. The larger nano-structuration, broader pore size distribution and very high He/Si atomic ratio (0.9 at the top) for sample 2 lead to a lower temperature for He release. Sample 3 with a lower He/Si atomic ratio, and a narrow pore size distribution centered at 11 nm, showed the higher thermal stability under vacuum. As already described the grazing incidence XRD analyses for as prepared films show in all cases no diffraction peaks as expected for the amorphous nature of the nanostructured Si films [16]. Fig. 8 shows the *in-situ* X-ray diffraction during annealing in vacuum for sample 1 fabricated on a fussed quartz amorphous substrate (see Table 2 for annealing details). Crystallization starts at ca. 1073 K when de diffraction of the (111) planes of crystalline Si can be clearly identified (according to JCPDS reference code: 00-027-1402). Therefore crystallization will happen long after the helium release.

For complementary *ex-situ* experiments the additional sample 4 was fabricated on Si and fussed quartz substrates at 150W in RF mode (Fig. S1). Fig. 9 shows its X-Ray diffractograms and p-EBS spectra before and after annealing in an inert (Helium) gas flow at selected temperatures of 573 and 823 K (see details in Table 2). Films for the p-EBS and XRD analyses were grown on Si and fussed quartz respectively. Annealing under the inert gas flow shows similar results as annealing in vacuum for sample 1 with the start of the He release at 573 K and no crystallization in the tested conditions limited to heating at 823 K.

### 3.3. Films characterization after thermal treatments

Samples 1 to 3 were analyzed by electron microscopy after annealing in the DIADDHEM setup leading to the in-situ analyses shown in Fig. 7. Top-view SEM images are presented in Fig. 10 where we can observe a stronger blistering effect after total He desorption for sample 2, which is also the one showing the lower temperature for He release. This may be related to the presence of bigger pores in the as prepared film, together with the higher nanostructuration and relatively very high He content in the top layer. From ion implanted samples it was also observed that blisters can form at boundaries by absorbing nearby cavities. Blisters can burst, leaving behind a denude zone [28]. As we can observe in Fig. 10 blistering is also observed in sample 1 but less abundant. However for sample 3 (grown with $^{3}$He in RF) blistering is rarely observed. In this particular case the top-view SEM image at high magnification shows a textural change that could be associated to delamination occurring during He desorption by annealing. This effect is also expected considering that thin films of Si can be fabricated by proton and helium implantation followed by annealing and thin film exfoliation [48]. The size of the pores and the total amount of He (lower and homogeneously distributed) in sample 3 appears to favor a controlled He release showing delamination rather than blistering.

For the silicon supported films after the *in-situ* annealing we have remaining thickness and/or large areas out of the blisters to achieve TEM cross section preparations. Therefore representative TEM images after annealing are shown in Fig. 11 showing the remanence of the porous nanostructure after He out-diffusion. These results are also of interest considering the fabrication of porous nanostructures based on

the He assisted magnetron sputtering technique.

## 4. Conclusions

Based on previous works selected conditions have been used to fabricate $^{4}$He and $^{3}$He charged Si–He nanocomposite amorphous films by magnetron sputtering deposition. The integration of IBA analysis, electron microscopy and X-ray diffraction tools have shown to be fundamental to elucidate microstructure and composition including in-depth profile analysis. A first important conclusion is that contaminants, mainly hydrogen and oxygen, favor He diffusion and release during films growth thus reducing the amount of trapped He. It was also demonstrated that in the here selected conditions DC operation mode account for increased surface nanostructuration and a broader bubbles size distribution as compared to the RF mode. These effects appear associated to a higher substrate temperature during film deposition.

For a practical use it is important to elucidate the prevalence of structure and composition of the He loaded films. The ex-situ and in-situ analysis of He content evolution under annealing was supported by XRD and electron microscopy studies. Temperatures of 573 and 723 K could be reached before He releases in the annealing conditions of this work for samples containing 32 and 29 at% of He. Blistering and delamination have been proved to be major annealing effects limiting the fabrication of He-free porous structures. A previous work reported He release at 1500 K for W films growth by MS in He although for a much lower He/W ratio of 0.087 [49].

Regarding He content most favorable conditions lead in this work to a maximum He/Si atomic ratio of 0.9 which, to our knowledge, is the highest value reported up to know. Such a high amount of helium compromises the mechanical stability of the material with increased brittleness and a strong blistering effect under thermal treatment.

The presented study is relevant in the context of proposed applications mainly related to the solid-gas nanocomposite character of the materials. The microstructure elucidation and depth profile compositions are fundamental information for a practical use of these films as solid targets for nuclear reaction studies. These applications include targets for scattering cross sections measurements and studies in inverse kinematic configuration [22–25]. In addition the thermal stability and the capacity to get nanoporous materials during fabrication, or after controlled helium release by annealing, are also of interest in fields related to optical applications [18], catalysis/electrocatalysis [50], hydrogen production [21] or batteries [27]. In summary this work presents valuable characterization and know-how to further develop these materials.

## CRediT authorship contribution statement

**A. Fernández:** Funding acquisition, Investigation, Supervision, Conceptualization, Writing – original draft, Writing – review & editing. **T. Sauvage:** Investigation, Methodology, Data curation, Conceptualization, Writing – review & editing. **B. Diallo:** Investigation, Methodology, Data curation. **D. Hufschmidt:** Investigation, Methodology. **M.C. Jiménez de Haro:** Investigation, Visualization. **O. Montes:** Investigation. **J.M. Martínez-Blanes:** Investigation, Visualization. **J. Caballero:** Investigation, Visualization, Methodology. **V. Godinho:** Investigation, Writing – review & editing. **F.J. Ferrer:** Investigation, Writing – review & editing. **S. Ibrahim:** Investigation, Writing – review & editing. **P. Brault:** Supervision, Writing – review & editing. **A.-L.- Thoman:** Funding acquisition, Supervision, Writing – review & editing.

## Declaration of competing interest

The authors declare that they have no known competing financial interests or personal relationships that could have appeared to influence the work reported in this paper.

## Data availability

Data will be made available on request.

## Acknowledgements

This work was supported by the Spanish and Junta de Andalucía grants no. RTI2018-093871-BI00, P20-00239 and PID2021-124439NB-I00 (all co-financed by EU FEDER) and the CSIC grant 202160E029. We acknowledge the French EMIR&A network for provision of irradiation beam time and assistance in using the CEMHTI-Pelletron facility. This work was also supported by the region of « Centre Val de Loire » and the European Regional Development Funds (FEDER). The authors also thank LE STUDIUM Loire Valley Institute for Advanced studies. We acknowledge the assistance of I. Rosa for the cross section TEM lamellas preparation and Olivier Wendling for technical support during IBA analyses.

## Appendix A. Supplementary data

Supplementary data to this article can be found online at https://doi.org/10.1016/j.matchemphys.2023.127674.

## References

[1] H. Ullmaier, The influence of helium on the bulk properties of fusion reactor structural materials, Nucl. Fusion 24 (1984) 1039.
[2] A.A. Lucas, Helium in metals, Phys. B+C 127 (1984) 225–239.
[3] X. Sun, F. Chen, H. Huang, J. Lin, X. Tang, Effects of interfaces on the helium bubble formation and radiation hardening of an austenitic stainless steel achieved by additive manufacturing, Appl. Surf. Sci. 467–468 (2019) 1134–1139, https://doi.org/10.1016/j.apsusc.2018.10.268 [doi:.
[4] T.J. Petty, J.W. Bradley, Tungsten nanostructure formation in a magnetron sputtering device, J. Nucl. Mater. 453 (2014) 320–322, https://doi.org/10.1016/j.jnucmat.2014.07.023 [doi:.
[5] Nishijima Dai, M.Y. Ye, N. Ohno, S. Takamura, Formation mechanism of bubbles and holes on tungsten surface with low-energy and high-flux helium plasma irradiation in NAGDIS-II, J. Nucl. Mater. (2004) 329–333, https://doi.org/10.1016/j.jnucmat.2004.04.129, 1029–1033. [doi]:.
[6] L. Pentecoste, P. Brault, A.-L. Thomann, P. Desgardin, T. Lecas, T. Belhabib, M.-F. Barthe, T. Sauvage, Low energy and low fluence helium implantations in tungsten: molecular dynamics simulations and experiments, J. Nucl. Mater. 470 (2016) 44–54, https://doi.org/10.1016/j.jnucmat.2015.12.017 [doi:.
[7] S.E. Donnelly, J.H. Evans (Eds.), "Fundamental aspects of inert gases in solids", Springer Science+Business Media New York © 1991, Plenum Press, New York, 1991, https://doi.org/10.1007/978-1-4899-3680-6. Originally published by.
[8] X. Gai, R. Smith, S.D. Kenny, Inert gas bubbles in bcc Fe, J. Nucl. Mater. 470 (2016) 84–89.
[9] E.L. Fleischer, M.G. Norton, Noble gas inclusions in materials, Heterog. Chem. Rev. 3 (3) (1996) 171–201.
[10] S. Takamura, N. Ohno, D. Nishijima, S. Kajita, formation of nanostructured tungsten with arborescent shape due to helium plasma irradiation, Plasma Fusion Res. 1 (2) (2006) 51.
[11] S. Takamura, Y. Uesugi, Experimental identification for physical mechanism of fiber-form nanostructure growth on metal surfaces with helium plasma irradiation, Appl. Surf. Sci. 356 (2015) 888–897, https://doi.org/10.1016/j.apsusc.2015.08.112 [doi:.
[12] J.P. Jia, L.Q. Shi, X.C. Lai, Q.F. Wang, Preparation of Al thin films charged with helium by DC magnetron sputtering, Nucl. Instrum. Methods Phys. Res. B 263 (2007) 446–450, https://doi.org/10.1016/j.nimb.2007.06.022 [doi:.
[13] L.Q. Shi, C.Z. Liu, S.L. Xu, Z.Y. Zhou, Helium-charged titanium films deposited by direct current magnetron sputtering, Thin Solid Films 479 (2005) 52–58.
[14] H. Zheng, S. Liu, H.B. Yu, L.B. Wang, C.Z. Liu, L.Q. Shi, Introduction of helium into metals by magnetron sputtering deposition method, Mater. Lett. 59 (2005) 1071–1075, https://doi.org/10.1016/j.matlet.2004.12.008.
[15] E.-A. Kouadri-boudjelthia, E. Ntsoenzok, R. Benoit, G. Regula, H. Etienne, T. Michel, S. Ashok, Plasma immersion ion implantation: a viable candidate for low cost purification of mc-Si by nanocavities, Nucl. Instrum, Methods Phys. Res. Sect. B 366 (2016) 150–154.
[16] V. Godinho, J. Caballero-Hernández, D. Jamon, T.C. Rojas, R. Schierholz, J. García-López, F.J. Ferrer, A. Fernández, A new bottom-up methodology to produce silicon layers with a closed porosity nanostructure and reduced refractive index, Nanotechnology 24 (10pp) (2013), 275604, https://doi.org/10.1088/0957-4484/24/27/275604.
[17] R. Schierholz, B. Lacroix, V. Godinho, J. Caballero-Hernández, M. Duchamp, A. Fernández, STEM–EELS analysis reveals stable high density He in nanopores of amorphous silicon coatings deposited by magnetron sputtering, Nanotechnology 26 (2015), 075703, https://doi.org/10.1088/0957-4484/26/7/075703.

[18] V. Godinho, T.C. Rojas, A. Fernández, Magnetron sputtered a-SiOxNy thin films: a closed porous nanostructure with controlled optical and mechanical properties, Microporous Mesoporous Mater. 149 (2012) 142–146, https://doi.org/10.1016/j.micromeso.2011.08.018 [doi:.
[19] B. Lacroix, V. Godinho, A. Fernández, Nitrogen nanobubbles in a-SiOxNy coatings: evaluation of its physical properties and chemical bonding state by spatially resolved EELS, J. Phys. Chem. C 120 (2016) 5651–5658, https://doi.org/10.1021/acs.jpcc.5b09036 [DOI:.
[20] B. Lacroix, V. Godinho, A. Fernández, The nanostructure of porous cobalt coatings deposited by magnetron sputtering in helium atmosphere, Micron 108 (2018) 49–54, https://doi.org/10.1016/j.micron.2018.02.004.
[21] S. Ibrahim, F. Zahrae Lahboub, P. Brault, A. Petit, A. Caillard, E. Millon, T. Sauvage, A. Fernández, Anne-Lise Thoman, Influence of helium incorporation on growth process and properties of aluminum thin films deposited by DC magnetron sputtering, Surf. Coating. Technol. 426 (8pp) (2021), 127808, https://doi.org/10.1016/j.surfcoat.2021.127808.
[22] V. Godinho, F.J. Ferrer, B. Fernández, J. Caballero-Hernández, J. Gómez-Camacho, A. Fernández, Characterization and validation of a-Si magnetron-sputtered thin films as solid He targets with high stability for nuclear reactions, ACS Omega 1 (2016) 1229–1238, https://doi.org/10.1021/acsomega.6b00270.
[23] G. Carozzi, J.J. Valiente-Dobón, A. Gadea, M. Siciliano, D. Mengoni, A. Fernández, V. Godinho, D. Hufschmidt, A. Di Nitto, Test of a 3He target for transfer reactions in inverse kinematics, Il Nuovo Cimento 42C (4 pp) (2019) 94, https://doi.org/10.1393/ncc/i2019-19094-9, art. nr.
[24] A. Fernández, D. Hufschmidt, J.L. Colaux, J.J. Valiente-Dobón, V. Godinho, M. C. Jiménez de Haro, D. Feria, A. Gadea, S. Lucas, Low gas consumption fabrication of 3He solid targets for nuclear reactions, Mater. Des. 186 (10pp) (2020), 108337, https://doi.org/10.1016/j.matdes.2019.108337.
[25] F.J. Ferrer, B. Fernández, J.P. Fernández-García, F.G. Barba, A. Fernández, D. Galaviz, V. Godinho, J. Gómez-Camacho, A.M. Sánchez-Benítez, Novel solid $^{4}$He targets for experimental studies on nuclear reactions: $^{6}$Li+$^{4}$He differential cross-section measurement at incident energy of 5.5 MeV, Eur. J. Phys. 135 (8pp) (2020) 465, https://doi.org/10.1140/epjp/s13360-020-00482-w.
[26] J. Caballero-Hernández, V. Godinho, B. Lacroix, M.C. Jiménez de Haro, D. Jamon, A. Fernández, Fabrication of optical multilayer devices from porous silicon coatings with closed porosity by magnetron sputtering, ACS Appl. Mater. Interfaces 7 (2015) 13889–13897, https://doi.org/10.1021/acsami.5b02356 [doi:.
[27] J. Sakabe, N. Ohta, T. Ohnishi, K. Mitsuishi, K. Takada, Porous amorphous silicon film anodes for high capacity and stable all-solid-state lithium batteries, Commun. Chem. 1 (9pp) (2018) 24, https://doi.org/10.1038/s42004-018-0026-y.
[28] S.-H. Li, J.-T. Li, W.-Z. Han, Radiation-induced helium bubbles in metals, Materials 12 (32pp) (2019) 1036, https://doi.org/10.3390/ma12071036.
[29] M.-A. Nguyen, M.-O. Ruault, F. Fortuna, Formation and growth of nanocavities and cavities induced by $He^{+}$ implantation in silicon, Adv. Nat. Sci. Nanosci. Nanotechnol. 3 (2012), 015015, https://doi.org/10.1088/2043-6262/3/1/015015 (5pp).
[30] N. Cherkashin, N. Daghbouj, G. Seine, A. Claverie, Impact of He and H relative depth distributions on the result of sequential $He^{+}$ and $H^{+}$ ion implantation and annealing in silicon, J. Appl. Phys. 123 (9pp) (2018), 161556, https://doi.org/10.1063/1.5012505.
[31] S. Frabboni, F. Corni, C. Nobili, R. Tonini, G. Ottaviani, Nanovoid formation in helium-implanted single-crystal silicon studied by in situ techniques, Phys. Rev. B 69 (9pp) (2004), 165209, https://doi.org/10.1103/PhysRevB.69.165209.
[32] F. Chamssedine, T. Sauvage, S. Peuget, DIADDHEM set-up: new IBA facility for studying the helium behavior in nuclear glasses, Nucl. Instrum. Methods Phys. Res. B 268 (2010) 1862–1866, https://doi.org/10.1016/j.nimb.2010.02.031 [doi:.
[33] A. Fernández, D. Hufschmidt, V. Godinho, M.C. Jiménez de Haro, Spanish patent application No. P201831107, Procedimiento de obtención de un material sólido con agregados gaseosos mediante pulverización catódica por magnetrón en condiciones estáticas o cuasiestáticas para reducir el consumo de gas, patent filed on 15 Nov 2018. [WO2020099695A1].
[34] W.S. Rasband, U. ImageJ, S. National, Institutes of health, bethesda, Maryland, USA. https://imagej.nih.gov/ij/, 1997–2018.
[35] M. Mayer, Improved physics in SIMNRA 7, in: 21st Int, Conf. Ion Beam Anal., 332, 2014, pp. 176–180, https://doi.org/10.1016/j.nimb.2014.02.056 [doi:.
[36] A.F. Gurbich, SigmaCalc recent development and present status of the evaluated cross-sections for IBA, Nucl. Instrum. Methods Phys. Res. Sect. B Beam Interact. Mater. Atoms 371 (2016) 27–32.
[37] www-nds.iaea.org/ibandl.
[38] J.S. Custer, M.O. Thompson, D.C. Jacobson, J.M. Poate, S. Roorda, C. Sinke, F. Spaepen, Density of amorphous Si, Appl. Phys. Lett. 64 (1994) 437–439, https://doi.org/10.1063/1.111121 [doi:.
[39] Institute for Applied Physics, Wien Tu, A simple sputtering yield calculator. https://www.iap.tuwien.ac.at/www/surface/sputteryield.
[40] A. Anders, A structure zone diagram including plasma-based deposition and ion etching, Thin Solid Films 518 (2010) 4087–4090, https://doi.org/10.1016/j.tsf.2009.10.145 [doi:.
[41] Q. Su, H. Ding, L. Price, L. Shao, J.A. Hinks, G. Greaves, S.E. Donnelly, M. J. Demkowicz, M. Nastasi, Rapid and damage-free outgassing of implanted helium from amorphous silicon oxycarbide, Sci. Rep. 8 (9pp) (2018) 5009, https://doi.org/10.1038/s41598-018-23426-y.
[42] G. Szakács, E. Szilágyi, F. Pászti, E. Kótai, Determination of migration of ion-implanted helium in silica by proton backscattering spectrometry, Nucl. Instrum. Methods B 266 (2008) 1382–1385, https://doi.org/10.1016/j.nimb.2007.12.002 [doi:.
[43] A. Manuaba, F. Pászti, A.R. Ramos, N.Q. Khánh, B. Pécz, Z. Zolnai, A. Tunyogi, E. Szilágyi, Effect of pre-implanted oxygen in Si on the retention of implanted He, Nucl. Instrum. Methods B 249 (2006) 150–152, https://doi.org/10.1016/j.nimb.2006.03.102 [doi:.
[44] W. Beyer, U. Zastrow, Helium effusion, diffusion and precipitation as a probe of microstructure in hydrogenated amorphous silicon, J. Non-Cryst. Solids 299–302 (2002) 254–258, https://doi.org/10.1016/S0022-3093(01)01004-3 [doi:.
[45] E. Oliviero, M.L. David, A.V. Fedorov, A. van Veen, M.F. Beaufort, J.F. Barbot, Helium implantation in silicon: the effects of implantation temperature, Materials, Science and Engineering B102 (2003) 222–227, https://doi.org/10.1016/S0921-5107(02)00736-5 [doi:.
[46] M.A. Nguyen, M.-O. Ruault, F. Fortuna, Formation and growth of nanocavities and cavities induced by He+ implantation in silicon, Adv. Nat. Sci. Nanosci. Nanotechnol. 3 (2012), 015015, https://doi.org/10.1088/2043-6262/3/1/015015 (5pp).
[47] K. Alix, M.-L. David, J. Dérès, C. Hébert, L. Pizzagalli, Evolution of the properties of helium nanobubbles during *in situ* annealing probed by spectrum imaging in the transmission electron microscope, Phys. Rev. B 97 (12pp) (2018), 104102, https://doi.org/10.1103/PhysRevB.97.104102.
[48] S. Reboh, A.A.D. de Mattos, F. Schaurich, P.F.P. Fitchner, M.F. Beauafort, J. F. Barbot, The mechanism of surface exfoliation in H and He implanted Si crystals, Scripta Mater. 65 (2011) 1045–1048, https://doi.org/10.1016/j.scriptamat.2011.09.012 [doi:.
[49] S. Iyyakkunnel, L. Marot, B. Eren, R. Steiner, L. Moser, D. Mathys, M. Düggelin, P. Chapon, E. Meyer, Morphological changes of tungsten surfaces by low-flux helium plasma treatment and helium incorporation via magnetron sputtering, ACS Appl. Mater. Interfaces 6 (2014) 11609–11616, https://doi.org/10.1021/am502370t.
[50] F. Giarratano, G.M. Arzac, V. Godinho, D. Hufschmidt, M.C. Jiménez, O. Montes, A. Fernández, Nanoporous Pt-based catalysts prepared by chemical dealloying of magnetron-sputtered Pt-Cu thin films for the catalytic combustion of hydrogen, Appl. Catal. B Environ. 235 (2018) 168–176, https://doi.org/10.1016/j.apcatb.2018.04.064 [doi:.